# Generating tensor-network states via combination of phonons and qubits in a trapped-ion platform

Si-Jing Tao,[1,2] Hao-Qing Zhang,[3,1,2] Hao Zhang,[1,2] Zhe Chen,[1,2] Ran He,[1,2] Shao-Jun Dong,[4] Yong-Jian Han,[1,2,4,*] Chuan-Feng Li,[1,2] and Guang-Can Guo[1,2]

[1]*Chinese Academy of Sciences Key Laboratory of Quantum Information, University of Science and Technology of China, Hefei 230026, People's Republic of China*

[2]*Chinese Academy of Sciences Center For Excellence in Quantum Information and Quantum Physics, University of Science and Technology of China, Hefei 230026, People's Republic of China*

[3]*Joint Institute for Laboratory Astrophysics, National Institute of Standards and Technology and Department of Physics, University of Colorado, Boulder, Colorado 80309, USA*

[4]*Institute of Artificial Intelligence, Hefei Comprehensive National Science Center, Hefei 230026, People's Republic of China*

(Received 12 May 2022; accepted 15 August 2022; published 2 September 2022)

Tensor-network (TN) states supply one of the most powerful variational tools to simulate quantum many-body systems. Though classical simulation of TN states (with approximation) is efficient, the required computational (classical) resources are still beyond our current capability when the size of the system and bond dimension becomes large (which is necessary for studying complicated quantum many-body systems). The TN contraction, which is the dominant cost in TN algorithms, can be replaced by measuring the corresponding physical observables directly in the experimentally prepared TN states. The computational cost is thus dramatically reduced. Here, we propose a scheme to generate TN states by combining multiple phonon modes and qubits in the ion trap platform. With the full connectivity and parallelism of the phonon modes operation, we can generate TN states with rough but complex entanglement structures [such as the multiscale entanglement renormalization *Ansatz* on the one-dimensional (1D) lattice and the projected entangled pair states on the kagome lattice] by shallow generation circuits. With the abundant local free parameters of the qubits operation, we can refine the local details of the generated TN states. We further benchmark the expressive power of the generated TN states by optimizing the ground energy, which is very close to the exact results of the 1D transverse-field Ising model near the critical point and the 1D Heisenberg model. Our method supplies a quantum-classical hybrid way to simulate the ground states of many-body systems and paves a promising way to demonstrate the advantage of quantum simulation.

DOI: 10.1103/PhysRevA.106.032403

## I. INTRODUCTION

The ground states play an essential role in exploring quantum many-body physics, such as quantum phase transition [1], spin liquid [2], and high-temperature superconductivity [3]. Among different ways to approach the ground states [4–10], the tensor-network (TN) method—a classical variational algorithm—has been proved as a powerful numerical tool [9,10]. Particularly, it has been proved that the ground state of a one-dimensional (1D) gapped local Hamiltonian system can be efficiently represented by the matrix product state (MPS) [11,12].

However, even though the complexity of the general TN algorithms only increases polynomially with the bond dimension $D$ used to measure the entanglement of the ground state [10] under some approximations [13–15], it is still very costly to simulate large many-body systems with complex entanglement structures. For example, the computational cost to simulate the projected entangled pair states (PEPS) in a two-dimensional (2D) bosonic system with open boundary condition (OBC) scales as $O(D^{10})$ [$D$ is usually of the order of $O(10)$ at least] [16–18]. The situation will be even worse in the fermionic systems due to the violation of the entanglement entropy area law [19] which requires the larger $D$ to keep the calculation accuracy.

In the general TN algorithms, the most costly part is to contract the whole tensor network to obtain the observable expectation. On the other hand, the contraction of TN can be done automatically by measuring the corresponding observables on the same TN states generated in the experiments. Therefore, the contraction of the TN state can be transformed to the efficient generation of powerful TN states in physical platforms.

Recently, a lot of schemes to generate TN states have been proposed for different platforms, such as cavity-QED [20,21], waveguide-QED [22], atomic array [23], circuit-QED [24], optics [25–27], and trapped ion [28–30]. However, since all of the schemes are based on sequential unitary operations, the flexibility of the generated TN states is limited to the 1D MPS [20–24,26,31,32] and 2D PEPS on the square lattice [24,25,27,33]; consequently, their expressive power is limited.

*smhan@ustc.edu.cn

 

Particularly, the multiscale entanglement renormalization *Ansatz* (MERA), which can be used to simulate states with entanglement beyond area law such as the ground state of a system near the critical point [34,35] and has a deep relationship with the holographic theory [35,36], cannot be generated by the sequential way; also the PEPS state on the kagome lattice [2,37–39], which is the natural *Ansatz* to simulate the ground state of the quantum system on the kagome lattice, cannot be generated by this method.

The trapped-ion system is one of the most promising systems for quantum computing [40–43]. Besides encoding quantum information onto the qubit degree of freedom [40,44–48], the hybrid phonon and spin system [49] have attracted a lot of attention in quantum simulation [49–56] and error correction [57–59]. Quantum operations between multiple motional modes (either local modes [60–64] or collective modes [55,65–69]) and between qubits (either one-qubit gate or two-qubit gate [40,44–48,70]) have been much improved recently. Recent developments in high optical access ion traps [71] give the ability for addressing and operating ions with much freedom.

Based on these technologies, in this paper, we propose a scheme to generate TN states by combining the phonon modes and qubits in the ion trap. Due to the full connectivity and parallelism of the operations between two phonon modes, the generated TN states are more flexible than by the previous scheme [21–24,26,27,31,32]. Particularly, the MERA on the 1D lattice and the PEPS on the kagome lattice can be generated, and the TN states which can be generated by the previous scheme such as the MPS can be generated within much fewer steps. Moreover, with the abundant free parameters of the qubit operations, we can refine the local details of the generated TN states, which improves the expressive power of the states. To benchmark the expressive power of the TN states generated in our scheme, we use them to optimize the ground-state energies of the 1D Heisenberg model and the 1D transverse-field Ising model near the critical point. Comparing them with the exact results, their differences are within 1%, which explicitly shows that the TN states generated by our scheme are powerful enough to simulate the ground states of these quantum many-body systems.

## II. THEORETICAL BACKGROUND

### A. Tensor-network state and its application

Generally, a quantum state in a $n$-qudit system can be exactly expressed as

$$|\psi\rangle = \sum_{s_1,s_2,\ldots,s_n} C_{s_1,s_2,\ldots,s_n}|s_1, s_2, \ldots, s_n\rangle \tag{1}$$

where $C_{s_1,s_2,\ldots,s_n}(s_1, s_2, \cdots, s_n \in \{1, 2, \cdots, d\})$ is the amplitude of basis $|s_1, s_2, \ldots, s_n\rangle$ and they form a rank-$n$ tensor which can be represented as a diagram shown in Fig. 1(a). Unfortunately, the number of coefficients (free parameters) in the quantum states is increasing exponentially with the number of qudits. This fact leads to the intractability of solving quantum many-body systems problems through the exact diagonalization method in classical computers. Besides the Monte Carlo method with the notorious sign problem in the frustrated system and fermionic systems [4,5], the variational method is the main method to overcome the "exponential wall" problem by only focusing on the special subspace of the whole Hilbert. Different *Ansätze* have been proposed for many-body systems, such as Hartree-Fock [6], Gutzwiller function [7,8], and TN states [9,10], among which the TN states have been proved as powerful tools for simulating strong-correlated systems.

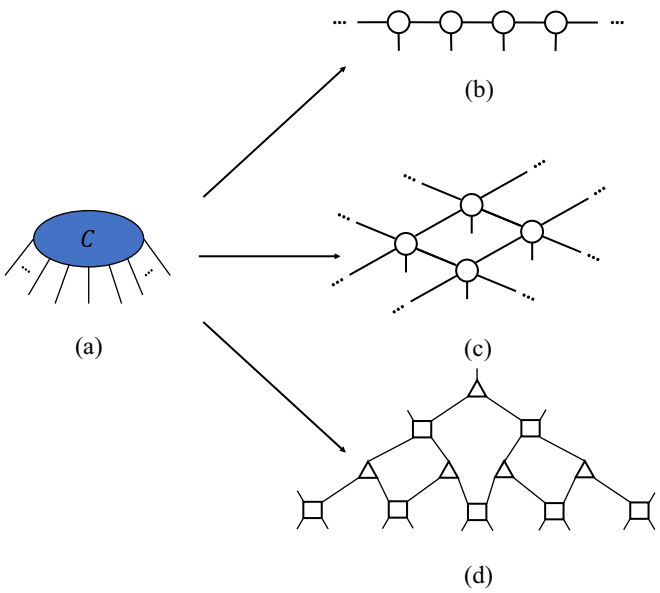


FIG. 1. (a) A rank-$n$ tensor for representing a general quantum state. (b) The TN diagram of the MPS. (c) The TN diagram of the PEPS on the square lattice. (d) The TN diagram of the MERA on the 1D lattice. The triangle denotes an isometry tensor and the square denotes a disentangler tensor.

The MPS [shown in Fig. 1(b)] is a 1D TN state which can be expressed as

$$|\psi_{\text{MPS}}\rangle = \sum_{s_1,\cdots,s_L} \text{Tr}[A^{s_1}(1)A^{s_2}(2)\cdots A^{s_L}(L)]|s_1 s_2 \cdots s_L\rangle, \tag{2}$$

where $L$ is the length of the 1D chain, $s_k = 1, 2, \cdots, d$ $(k = 1, 2, \ldots, L)$ is the physical index of site $k$, $A^s(k)$ is the tensor on site $k$ and chosen to be a $D \times D$ matrix for any given $s$, and $D$ is generally called the bond dimension (or Schmidt number) of the state $|\psi\rangle$ which is related with the entanglement of the state. Particularly, for OBC, $A^s(1)$ and $A^s(L)$ are $D$-dimensional vectors. With this form, the number of free parameters in the MPS is $O(LD^2d)$. Obviously, any quantum state can be approximated by a MPS form precisely if the parameter $D$ is big enough (exponentially increasing with the size $L$). When the parameter $D$ is limited to some fixed number, the states in Eq. (2) form a variational space (a part of the whole Hilbert space). Fortunately, it is proved that the ground state of the gapped local 1D system can be efficiently covered by this subspace [11]. As a result, the MPS is a powerful class of the variational states for the 1D quantum many-body system; actually, the variational *Ansatz* in the density-matrix renormalization-group method is a MPS [72].

Moreover, the MPS can be expressed in another way. As shown in Fig. 2(a), there are two virtual particles on each

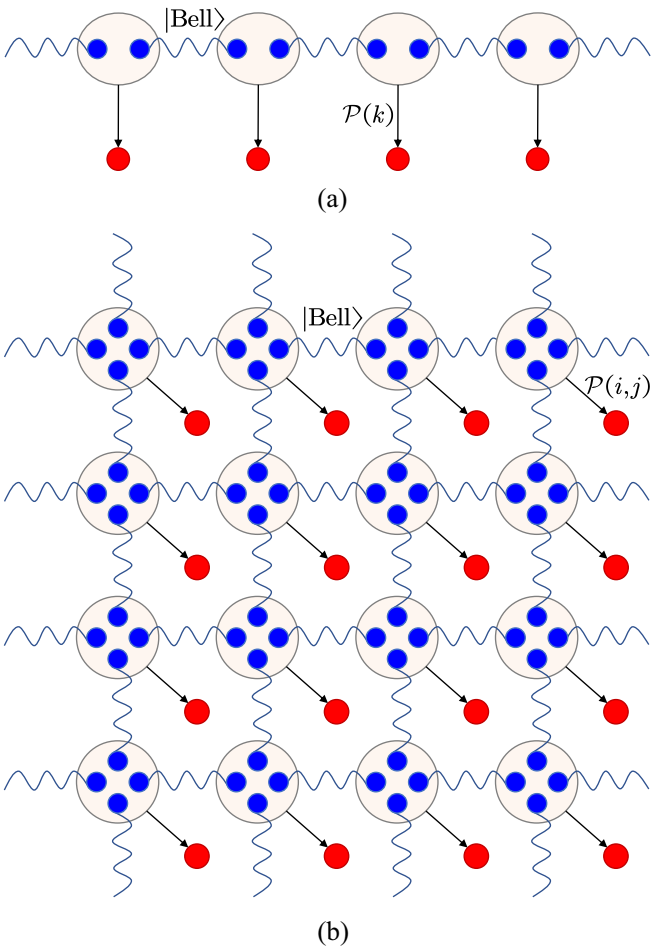


FIG. 2. The pair of blue dots connected by a wavy line represents the maximally entangled pair, $\mathcal{P}(k)$ and $\mathcal{P}(i,j)$ are the linear operators, and $|\text{Bell}\rangle$ is the Bell state. (a) Another expression of the MPS. (b) The PEPS on the square lattice.

site the Hilbert space of which is $D$ dimensional. For each edge connecting two nearest-neighbor site, we associate a maximally entangled state $|\text{Bell}\rangle = \frac{1}{D}(|0,0\rangle + |1,1\rangle + \cdots + |D-1, D-1\rangle)$ of two virtual particles (the pairs of the blue dots, one on each neighboring site, connected by a wavy line in Fig. 2). Then, we apply a linear operator on each site to project the two virtual particles on the same site to a physical space:

$$\mathcal{P}(k) = \sum_{s;l,r} A^s_{lr}(k)|s\rangle\langle l, r| \tag{3}$$

where $k$ is the site index, $s$ is the physical index, and $|l\rangle$ ($|r\rangle$) is the state of the left (right) virtual particle on the site $k$. With these notations, the MPS can be defined as

$$\begin{aligned}|\psi_{\text{MPS}}\rangle &= \prod_k \mathcal{P}(k) \bigotimes_e |\text{Bell}\rangle_e \\ &= \sum_{s_1,s_2,\cdots,s_L} \text{Tr}[A^{s_1}(1)A^{s_2}(2)\cdots A^{s_L}(L)]|s_1 s_2 \cdots s_L\rangle\end{aligned} \tag{4}$$

where $|\text{Bell}\rangle_e$ is the Bell state associated with the edge $e$ in the lattice, and $A^{s_k}(k)$ is a matrix on the site $k$ with index $s_k$ formed by the tensor $A^{s_k}_{l,r}(k)$.

By generalizing this idea, we can define the higher-dimensional TN state—the PEPS [9,17,73]. Taking the PEPS on the square lattice as an example, as shown in Fig. 2(b), we align a maximally entangled pair to each edge of a square lattice, and then we apply a linear projector to each site:

$$\mathcal{P}(i,j) = \sum_{s;u,l,d,r} A^s_{uldr}(i,j)|s\rangle\langle u, l, d, r|, \tag{5}$$

where $(i,j)$ denotes the location of the operator, and $|u\rangle$, $|l\rangle$, $|d\rangle$, and $|r\rangle$ denote the state of the upper, left, down, and right virtual particles on the site $(i,j)$. Finally, the PEPS on the $L_1 \times L_2$ square lattice is defined as

$$\begin{aligned}|\psi_{\text{PEPS}}\rangle &= \prod_{i,j} \mathcal{P}(i,j) \bigotimes_e |\text{Bell}\rangle_e \\ &= \sum_{s_{(1,1)},s_{(1,2)},\ldots,s_{(L_1,L_2)}} \text{Contr}[A^{s_{(1,1)}}(1,1)A^{s_{(1,2)}}(1,2)\cdots \\ &\quad \times A^{s_{(L_1,L_2)}}(L_1,L_2)]|s_{(1,1)}, s_{(1,2)}, \ldots, s_{(L_1,L_2)}\rangle\end{aligned} \tag{6}$$

where $|\text{Bell}\rangle_e$ is the Bell state associated with the edge $e$, $A^s(i,j)$ is a tensor formed by the element $A^s_{u,l,d,r}(i,j)$ on site $(i,j)$, and $\text{Contr}(\cdot)$ means contraction of the tensor network.

The MPS and the PEPS satisfy the area-law scaling of the entanglement entropy [9]. However, for some systems, such as the fermionic systems [19] and the systems near the critical points [34], the entanglement of their ground states is beyond the area law. As a result, the bond dimension $D$ for the PEPS to approach certain accuracy for the ground states will increase with the system size, which is not efficient for classical computation. Some more complicated TN states are required.

The MERA [34,74], the scaling of which of the entanglement can be beyond the area law, has been proposed to calculate some complicated ground states, such as the ground states of the systems near the critical point [34,35]. The TN representation of the MERA on a 1D lattice is shown in Fig. 1(d). By definition [34,74], the MERA on a 1D lattice consists of two kinds of tensor—isometry tensor (triangle) and disentangler tensor (square). Besides, recent works point out that the MERA has some relationship with holography [35,36], which is one of the most important directions of quantum gravity [75,76].

### B. Difficulty of the TN algorithm

With a given TN state *Ansatz* (fixed parameters $D$), the main task of the TN algorithm is to optimize the parameters to approach the target state such as the ground state of the quantum many-body system. There are two main methods to optimize the free parameters of the TN: one is based on the gradient descent method and the other is based on imaginary time evolution [17,77]. For both methods, the final physical results must be obtained by calculating the expectation value of physical observables, which is completed by contracting the whole tensor network. Even though the complexities of the exact contraction of the MPS and the MERA on the 1D lattice are $O(D^3)$ [10] and $O(D^9)$ [10,74], respectively, they are thus efficient for classical computers. However, generally,

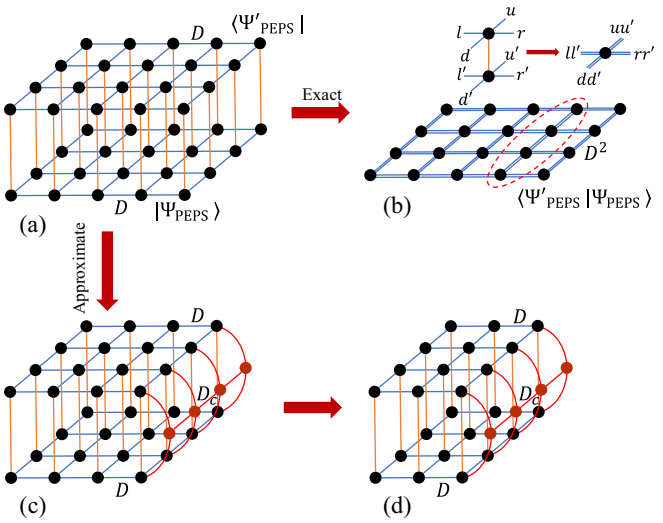


FIG. 3. The blue line is the virtual lag of the PEPS, the orange line is the physical lag of the PEPS, and $D$ is the bond dimension of the PEPS on the square. (a) The calculation of $\langle\Psi'_{\text{PEPS}}|\Psi_{\text{PEPS}}\rangle$. (b) The exact contraction of the TN in (a). The contraction between the tensor $A_{lrud,s}$ and $A_{l'r'u'd',s'}$ would be tensor $T_{ll',rr',uu',dd'}$. (c, d) The approximated contraction of the TN in (a) by the matrix product operator (MPO) compression approximation method. The red part is the MPO where $D_c$ is the bond dimension cut of the MPO.

the exact contraction of the tensor network in two dimensions will result in the exponential increase of the resource with the system size. Taking the exact contraction of $\langle\Psi'_{\text{PEPS}}|\Psi_{\text{PEPS}}\rangle$ on the $L \times L$ square lattice as an example [as shown in Figs. 3(a) and 3(b)], we have the following.

(1) For each site, contract the physical index of the tensor $A^s(i,j)$ (upper part) and $A^{*s'}(i,j)$ (lower part) to form a rank-8 tensor with element $T_{ll',rr',uu',dd'}(i,j)$, then combine the index $u$ and $u'$, $l$ and $l'$, $d$ and $d'$, and $r$ and $r'$ to form a $D^2 \times D^2 \times D^2 \times D^2$ tensor $T(i,j)$. The $L^2$ new tensors $T(i,j)$ form a new tensor network as shown in Fig. 3(b).

(2) After contracting the tensors $T(i,j)$ on each column, we get the $D^{2L} \times D^{2L}$ matrix except for the boundary column which is a $D^{2L} \times 1$ vector (under OBC). Obviously, it leads to exponential increment of the calculation time and storage.

Actually, the exact contraction of the PEPS is the #P-complete problem [78].

Because of the difficulty we discussed above, different approximated contraction methods are introduced, such as the tensor-entanglement renormalization group [13], and the matrix product operator (MPO) compression approximation method [14,15]. Based on these approximation methods, the contraction of the TN state can be implemented efficiently, i.e., we can complete TN contraction with polynomial scaling time and storage. For example, we can efficiently calculate the above case with the MPO compress approximation method as shown in Figs. 3(a), 3(c) and 3(d).

(1) We contract the tensor in the first column of the upper part and lower part to get a MPO [the red part in Figs. 3(c) and 3(d)] the bond dimension of which is $D^2$.

(2) We make the contraction between the MPO and the tensors in the next column, and get a new MPO with bond dimension $D^4$.

(3) To prevent the exponential increasing of the bond dimension, we should truncate the bond dimension to $D_c$ (usually set as $D_c = D^2$); in other words, we use a MPO with bond dimension $D_c$ to approximate the tensor network obtained in step 2.

(4) Repeat step 2 and 3 until all columns are contracted.

By this approximation, we would finally reduce the complexity of the contraction of the TN to $O(D^4 D_c^3 + D^6 D_c^2)$ where $D_c$ is the bond dimension cut [18]. Inserting $D_c = D^2$ (usual setting), the complexity of the contraction of the PEPS on the square lattice is usually $O(D^{10})$.

### C. General rules for tensor-network state generation

Though the calculation based on the TN state can be completed efficiently after doing approximation, however, the scaling [$O(D^9)$ for the 1D MERA [10,35] and $O(D^{10})$ for PEPS on the 2D lattice [16–18]] is still very high and makes the calculation cost still beyond our current capability when the bond dimension $D$ is large. Specifically, according to the recent result [79], $10^7$ heterogeneous cores on Sunway Taihu-Light are used to calculate the ground state of a 2D quantum system on a $24 \times 24$ open square lattice by using PEPS with bond dimension only $D = 16$.

With the development of quantum technologies, we have stepped into the noisy intermediate-scale quantum era (NISQ). It is possible to generate large-scale TN states in the experimental platform. Replacing the contraction process in the classical computation with measuring the same local physical quantities in the prepared corresponding TN state can dramatically reduce the computation complexity. Combining with the optimization in classical computers, the advantage of quantum simulation can be achieved by this quantum-classical algorithm.

Generating high-quality TN states with sufficient expressive power is the key part of the quantum-classical algorithm. The basic idea for TN states generation is doing the mapping between the building blocks: the unitary in quantum simulation and the tensor in a tensor network. First, any unitary operation can be viewed as a tensor; particularly, for a two-body unitary operation, we have

$$V = \sum_{o_1,o_2,i_1,i_2} V_{i_1 i_2}^{o_1 o_2} |o_1, o_2\rangle\langle i_1, i_2|, \tag{7}$$

where $V_{i_1 i_2}^{o_1 o_2}$ forms a rank-4 tensor which can be represented as the diagrams shown in Fig. 4(a). Second, the product between unitary operations corresponds to the contraction between the corresponding tensors. For example, the product between two-body unitary operations the quantum circuit of which is shown in Fig. 4(d) is

$$UV = \sum_{\substack{j_1,j_2;i_1,i_2 \\ o_1,o_2}} U_{i_1 i_2}^{j_1 j_2} V_{j_1,j_2}^{o_2 o_3} |o_1, o_2\rangle\langle i_1, i_2|, \tag{8}$$

where $\sum_{j_1,j_2} U_{i_1 i_2}^{j_1 j_2} V_{j_1,j_2}^{o_2 o_3}$ forms a rank-4 tensor which is the contraction result of two rank-4 tensors and can be represented as a diagram shown in Fig. 4(c). As a result of the universality of unitaries, any tensor-network state can be prepared with some fixed universal tensors (corresponding to a set of universal gates); however, the network may not be efficient.

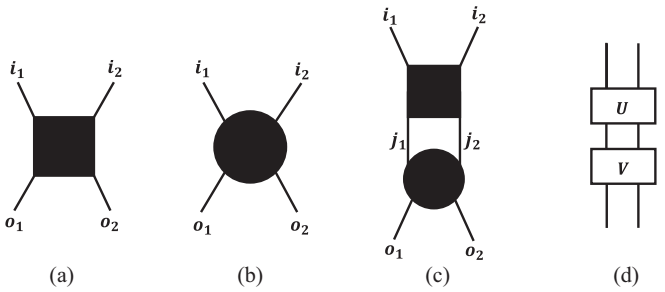


FIG. 4. (a, b) The TN diagram of the two phonon modes operation. (c) The TN diagram of the production between two two-mode operations. (d) The quantum circuit of the production of two two-mode operations.

Here, we focus on unitary gates with parameters, which are achievable with high quality in the current experimental setup, to generate variational tensor-network states and apply them to simulate the ground states of quantum many-body systems.

### D. Phonon-qubit tensor-network state generation scheme

Recently, different platforms have been introduced to generate TN-type quantum states [21–24,26,27,31,32]. These schemes to generate the TN state by sequential processes as an example are shown in Fig. 5. The sequential ways limit the entanglement structure of the TN states which limits the range of the ground states that can be simulated by the schemes, and requires very deep generation circuits which makes the outputs easily affected by the local noise of the unitary operation.

Actually, the two limitations above can be solved if the operation in the quantum simulator has the following advantages.

(1) *Full connectivity.* If the operation can be done between any pairs of the information units (such as phonon modes and qubits), the quantum circuits for generating TN states can be designed more freely than in previous schemes, which suggests TN states with more complex entanglement structures can be generated.

(2) *Parallelism.* If the operations between different pairs of the information units can be implemented simultaneously, the TN states can be generated by the shallow circuit. It suggests more robustness against the local noise in the circuit, which allows us to prepare a TN state in a larger system and larger $D$ (larger variational space).

Fortunately, the two-mode phonon operations in the ion trap have both of the advantages we stated above as we

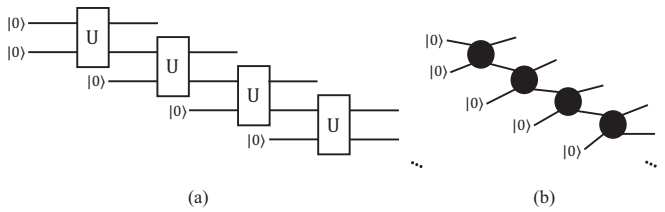


FIG. 5. (a) The quantum circuit for generating the MPS by the *Ansatz* in [26]. (b) The corresponding TN diagram of the quantum circuit in (a).

discussed in Sec. III. However, the number of the free parameters of the two-mode phonon operations is scarce (each operation has only two free parameters), which limits the expressive power of the generated TN states. In contrast to the two-mode phonon operation, the two-qubit operation has less connectivity since the coupling strength between two ions is limited by the power-law decay [80,81], and less parallelism since we need much fewer Raman beams to couple phonon pairs than to couple qubit pairs, which suggests less crosstalk noise but has much more free parameters.

In the following, we will introduce a scheme to generate TN states through the combination of the phonon modes and qubits in a trapped-ion system. With the full connectivity and parallelism of the phonon operation, we can generate complex TN states with rough entanglement structure by a shallow circuit, such as the MERA on a 1D lattice the entanglement scaling of which can be beyond the area law and the PEPS on the kagome lattice which is a geometrically frustrated lattice. With the abundant free parameters of the qubit operation, we can refine the local details of the generated TN states which improves their expressive power.

#### *1. Generation Ansätze for TN states with rough entanglement structure*

As examples, in the following, we will show how to generate different types of TN states based on the four-parameter experimentally realized two-mode unitary operators in the phonon modes of a trapped ion $U(\gamma,\psi,\theta,\phi) \equiv U(\mathbf{\Theta}) = U_{\mathrm{CMR}}(\theta,\phi)U_{\mathrm{TMS}}(\gamma,\psi)$ where $U_{\mathrm{CMR}}(\theta,\phi)$ and $U_{\mathrm{TMS}}(\gamma,\psi)$ are the collective modes rotation operation and two-mode squeezing operation separately.

*a. Matrix product state.* The MPS is one of the most simple but powerful TN states for the 1D many-body system [9,11,17]. Besides the sequential circuit in Fig. 5, the MPS can be generated by a shallow quantum circuit as shown in Fig. 6(a) in a trapped-ion system due to the parallelism of the phonon operation. It is clear that its depth is much smaller than the depth in the sequential circuit. Particularly, the circuits with depth 2 [all operations are two-mode unitary $U(\mathbf{\Theta})$ with different parameter values] are enough to generate a simple MPS. Obviously, the MPS can be generated by the quantum circuit with more layers [the example is shown in Fig. 6(c)], which gives the generated MPS more parameters and more entanglement (larger $D$), thus covering ground states of more many-body systems. Based on the mapping between the unitaries and the tensors, the TN diagram of the two-layer and four-layer generation circuit can be drawn as Figs. 6(b) and 6(d). To map the rank-6 tensor which is obtained by contracting the tensors in the red dashed circle or the red dashed polygon of Figs. 6(b) and 6(d) to the standard form in MPS, we need to fix the input legs (green legs) and view the output legs (orange legs) as physical legs as shown in Fig. 6(e). Generally, the input legs can be used as a parameter; however, for experimental convenience, we choose it as a vacuum state for every phonon mode.

*b. Projected entangled pair states.* Besides the MPS, the PEPS [9,16,73] on the square lattice and the kagome lattice can be generated in the following way.

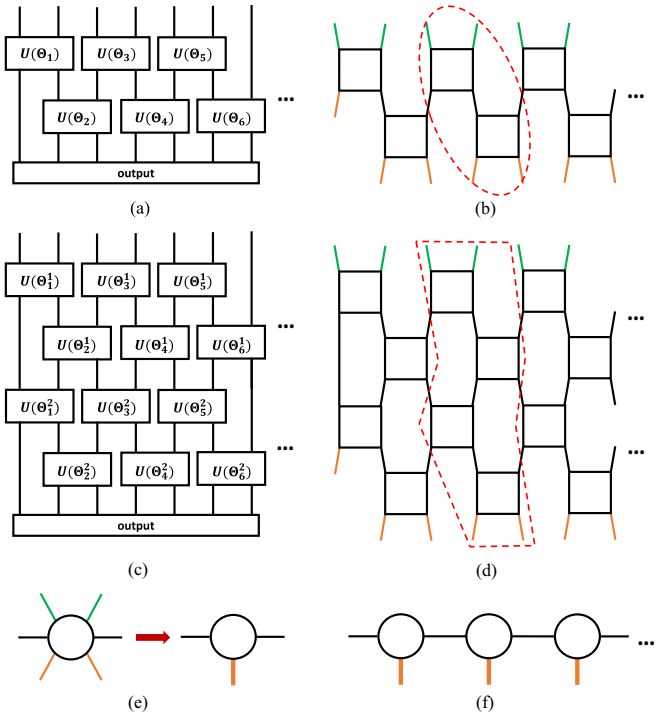


FIG. 6. The MPS *Ansatz* generation. The green legs are the input legs and the orange legs are the output legs. (a) The two-layer generation circuit for the MPS. (b) The TN diagram of the quantum circuit in (a). (c) The four-layer generation circuit for the MPS. (d) The TN diagram of the quantum circuit in (c). (e) The new rank-6 tensor by contracting the tensors in the red dashed circle in (b) or red dashed polygon in (d), and we get the form $A^s_{lr}$ in Eq. (2) after fixing the input parameters and combining two $d$-dimensional legs (orange line) into one $d^2$-dimensional leg (orange thick line). (f) The MPS TN diagram generated by the quantum circuit in (a) and (c).

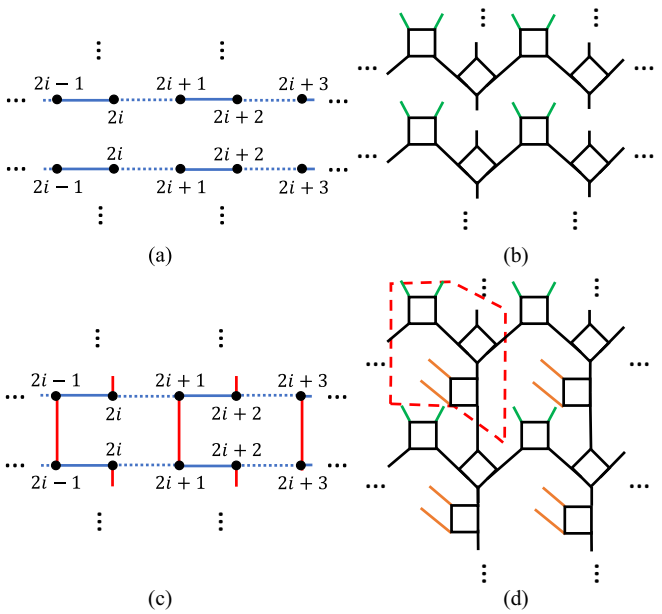


FIG. 7. The PEPS on the square lattice generation *Ansatz*. The left part is the operation steps for generating PEPS on the square lattice. The right part is the corresponding TN diagram of the left part. In the left diagrams, each black point represents one phonon mode, and we do the $U(\mathbf{\Theta})$ operation to the pair of the mode linked by the line. The same type of lines means the operation can be done simultaneously. In the right diagrams, the green legs are the input legs and the orange legs are output legs, and the white square with four legs represents the tensor of the operation $U(\mathbf{\Theta})$.

First, the PEPS on the $L \times L$ square lattice can be generated by the procedure shown in Fig. 7.

(1) We generate $L$ MPS chains [each has $2L$ phonon modes as shown in Figs. 7(a) and 7(b)] by the method we discussed before.

(2) Using four-parameter unitary operation $U(\mathbf{\Theta})$, we connect $L$ MPS chains to form a PEPS on a $L \times L$ lattice. Concretely, as shown in Figs. 7(c) and 7(d), the unitary $U(\mathbf{\Theta})$ is applied on the phonon mode $i$ ($i$ is odd) on the first and second MPS chain; when we add the third MPS chain to the $2 \times L$ PEPS, the unitary $U(\mathbf{\Theta})$ is applied on the phonon mode $j$ ($j$ is even) on the second and third MPS chain. Generally, when we add the $(k+1)$th MPS chain to the PEPS on the $k \times L$ lattice, if $k$ is odd (even), the unitary $U(\mathbf{\Theta})$ is applied on the odd(even)-numbered phonon mode on the $k$th and $(k+1)$th MPS chain. It is worth noting that all the unitary operations $U(\mathbf{\Theta})$ can be operated simultaneously when they act on different pairs of the modes.

To show the standard PEPS diagram, we contract the three connected tensors in the red dashed polygon of Fig. 7(d) to get a new rank-8 tensor shown in the panel of Fig. 9. By fixing the input legs (green legs) of the rank-8 tensor (the vacuum state is chosen as an example) and considering the outputs legs (orange legs) as the physical leg, the tensor is transformed to the form $A^s_{uldr}$ in Eq. (6). Then, we get the PEPS on the square lattice the TN diagram of which is shown in Fig. 9(a). It is worth noting that the full connectivity of the phonon operation makes sure that the operations above can be done, and all operations can be completed within $a+1$ steps because of the parallelism. Here $a$ is the number of steps to generate the MPS chains (at least two steps as we stated above).

Second, the generation of a PEPS on the kagome lattice can be demonstrated in Fig. 8.

(1) The phonon modes are divided into groups; in each group, the phonon modes are arrayed into four rows (Fig. 8). There are $n$ pairs of phonon modes in the first and third rows, and a unitary $U(\mathbf{\Theta})$ with a different parameter is applied on each pair. A MPS with $2n$ pairs of phonon modes is generated in the second and fourth row with the previous method.

(2) As shown in Figs. 8(c) and 8(d), in each group, three kinds of operations $U(\mathbf{\Theta})$ (each can have different parameters) are simultaneously used to entangle the modes in different rows. The first kind is operated between the right phonon mode of the $i$th pair in the first row and the right phonon mode of the $2i$th pair in the second row ($i = 1, 2, \ldots, n$); the second kind is operated between the left phonon mode of the $(2i-1)$th pair in the second row and the left phonon mode of the $i$th pair in the third row; and the third kind is operated between the right phonon mode of the $i$th pair in the third row and the right phonon mode of the $(2i-1)$th pair in the fourth row.

(3) As shown in Figs. 8(e) and 8(f), in each group, another three kinds of operations $U(\mathbf{\Theta})$ (each with different

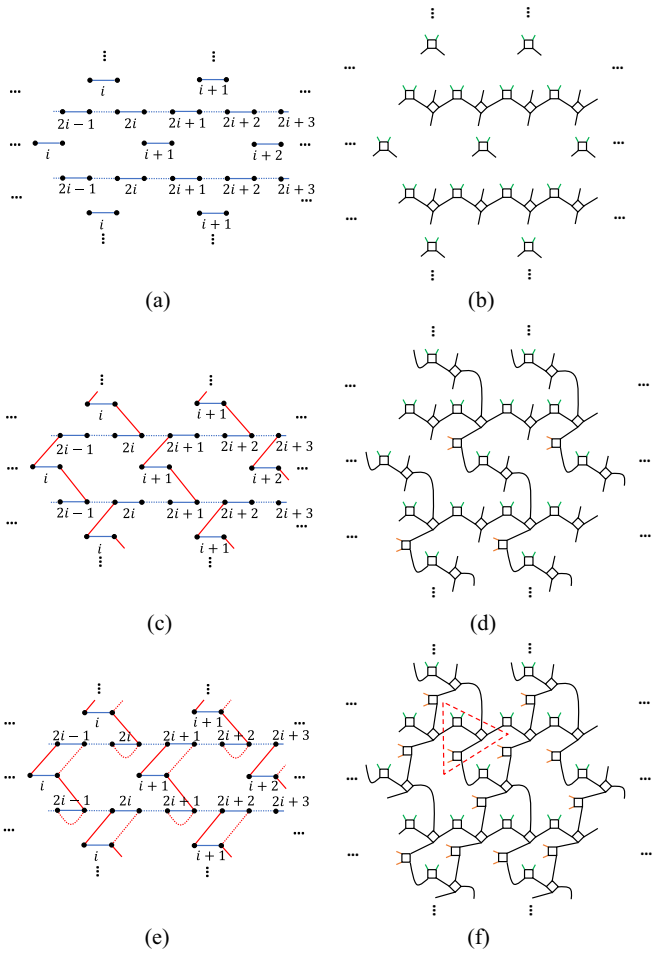


FIG. 8. The PEPS on the kagome lattice generation *Ansatz*. The left part is the operation steps for generating PEPS on the kagome lattice. The right part is the corresponding TN diagram of the left part. In the right diagrams, the green legs are the input legs and the orange legs are the output legs, and the white square with four legs represents the tensor of the operation $U(\boldsymbol{\Theta})$. In the left diagrams, each point represents one phonon mode, and we do the $U(\boldsymbol{\Theta})$ operation to the pair of the mode connected by the line. The same type of lines means the operation can be done simultaneously.

parameters) are also simultaneously used to refine the entanglement structure of the modes. The first kind is operated between the right phonon mode of the $(2i-1)$th pair in the second row and the right phonon mode of the $i$th pair in the third row; the second kind is operated on the even-numbered pairs of the phonon modes in the second row; and the third kind is operating on the odd-numbered pairs of the phonon modes in the fourth row.

(4) As shown in Figs. 8(c) and 8(e), by doing the $U(\boldsymbol{\Theta})$ operation between the left phonon mode of the $i$th pair in the first row of the lower group and the left phonon mode of the $2i$th pair in the fourth row of the upper group, and between the right phonon mode of the $2i$th pair in the fourth row of the upper group and the right phonon mode of the $i$th pair in the first row of the lower group, we can connect two groups together. Each nearest-neighbor group can be connected in this way.

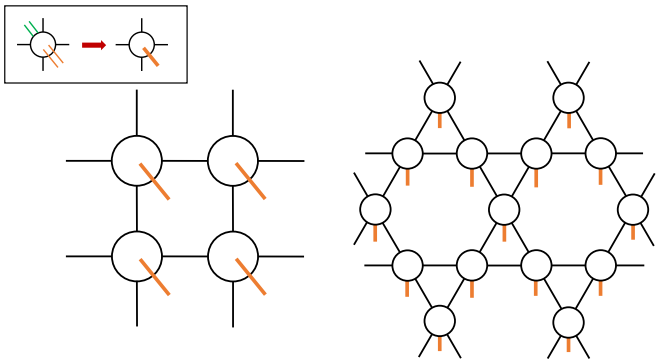


FIG. 9. (a) The TN diagram of the PEPS on the square lattice generated by the steps shown in Fig. 7. The tensor diagram in the panel is the new rank-8 tensor by contraction the three connected tensors in the red dashed polygon in Fig. 7(d) or the red dashed triangle in Fig. 8(f), and we get the tensor $A^s_{uldr}$ in Eq. (6) after fixing the input parameters and combining two $d$-dimensional legs (orange line) into one $d^2$-dimensional leg (orange thick line). (b) The TN diagram of the PEPS on the kagome lattice generated by the steps shown in Fig. 8.

The tensors in the red dashed triangle of Fig. 8(f) can be contracted to be a rank-8 tensor. Following the same process above, we get the PEPS on the kagome lattice the TN diagram of which is shown in Fig. 9(b). It is worth noting that the key reason we can do the operations above is the full connectivity of the phonon operation, and all operations can be completed with depth $a+2$ because of its parallelism, where $a$ is the number of steps used to generate the MPS chains (at least two steps as we stated above).

*c. Multiscale entanglement renormalization Ansatz.* It is very amazing, compared with other schemes [20–24,24–27,31–33], that our TN state generator can generate the MERA TN state. According to [34,35], the MERA TN consists of two kinds of tensors: one is the isometry tensor and another is the disentangler tensor. In the following, we take the MERA on a 1D lattice as an example. The disentangler tensor directly corresponds to a unitary operation, and the isometry tensor can be realized by a unitary operation with one input fixed to $|0\rangle$. As a result, a MERA on the 1D lattice shown in Fig. 10(b) can be generated by the quantum circuit shown in Fig. 10(a) which utilizes the parallelism of the phonon operation. The generation steps are as follows.

(1) In the first isometry layer, we start with a phonon mode with state $|0\rangle$ and another phonon mode with state $|\phi_0\rangle$, then the unitary $U(\boldsymbol{\Theta})$ is applied to them.

(2) In the first disentangler layer, we add two new phonon modes $|\phi_0(1)\rangle$ and $|\phi_1(1)\rangle$; the unitary $U(\boldsymbol{\Theta})$ is applied on one of the outputs of the first isometry layer and the new one $|\phi_0(1)\rangle$, while another unitary $U(\boldsymbol{\Theta})$ is applied on another output and the new one $|\phi_1(1)\rangle$.

(3) In the $m$th isometry layer, for each output of the upper layer, a unitary $U(\boldsymbol{\Theta})$ is applied to it and an additional phonon mode with state $|0\rangle$.

(4) In the $m$th disentangler layer, a unitary $U(\boldsymbol{\Theta})$ is operated on the two output modes from the nearest-neighbor

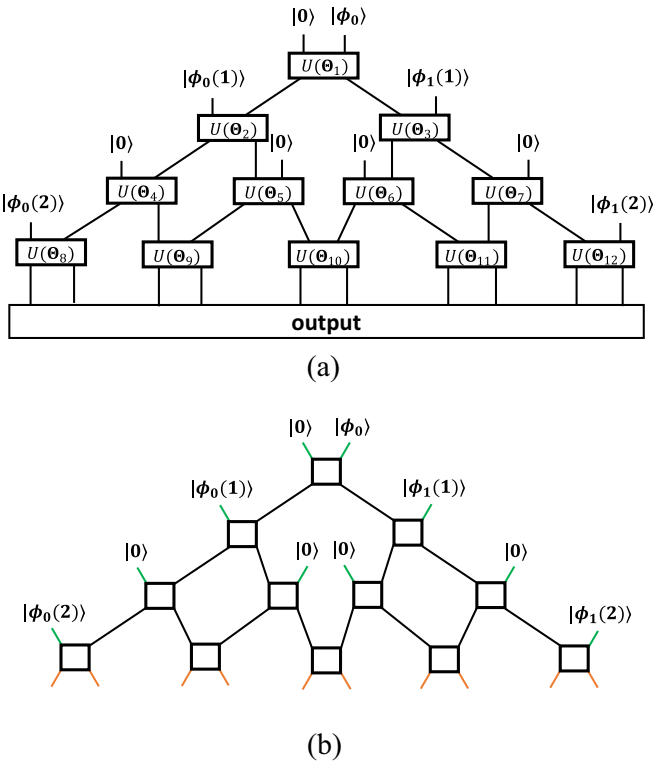


FIG. 10. The two-layer MERA TN state in the 1D generation *Ansatz*. The green legs are the input legs and the orange legs are the output legs. (a) The quantum circuit to generate the MERA TN state in one dimension. (b) The MERA TN diagram in one dimension generated by the quantum circuit in (a) where the tensor with one $|0\rangle$ input is the isometry tensor and the one without $|0\rangle$ is the disentangler tensor.

unitary (one for each) in the upper layer except for the boundary—at the left (right) boundary, one mode is from the upper left (right) boundary output and the other is from an additional mode with state $|\phi_0(m)\rangle$ [$|\phi_1(m)\rangle$].

With these operators, we can generate the desired MERA with depth $2L$ where $L$ is the number of the layers (one layer includes one isometry layer and one disentangler layer).

#### 2. *Improvement of local details of generated TN states*

The TN states with different entanglement structures can be generated by the *Ansätze* we stated before; however, because of the lack of the free parameters of the two-mode phonon operation, the entanglement structures of the generated TN states are rough, and their local details are not abundant enough to represent the state of the quantum many-body system, i.e., the expressive power of the generated TN states is low. Fortunately, the expressive power of the generated TN states can be improved with the help of the ion trap qubit. By the technique we will mention in the following Sec. III B, we can transfer the quantum information of the phonon modes (in the subspace of the Fock state $\{|0\rangle, |1\rangle\}$) to the ion qubit, and apply some local quantum gates to introduce many additional local parameters (the noise of local qubit operation can be controlled by the error mitigation or other postprocessing method). For example, as shown in Fig. 11,

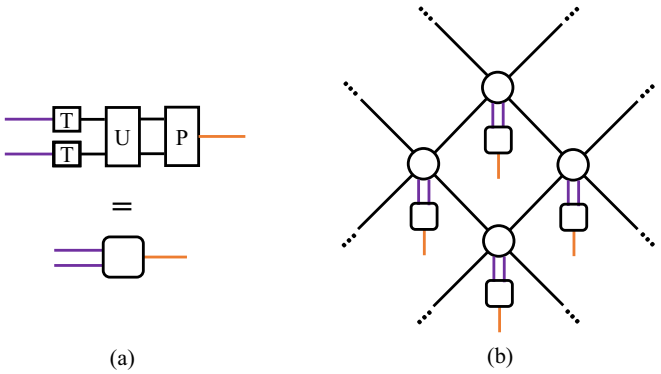


FIG. 11. (a) The square tensor with the "T" represents the operation by which we transfer the quantum information of the phonon mode in the phonon number subspace $\{|0\rangle, |1\rangle\}$ to the ion qubit. The square tensor with the "U" represents the two-qubit operation. The square tensor with the "P" represents the postprocessing which maps the output state into a multiple qubits state. (b) The PEPS on the square lattice generation *Ansatz*, where the orange legs are the output legs, and the purple legs are the connection legs between the phonon part and the qubit part.

after transferring the information from phonon modes to the qubits, a layer of local two-qubit gates is operated on the qubits, by which the number of the free parameters is improved (16 additional parameters in each two-qubit gate).

## III. EXPERIMENT TOOLBOX

In this part, we discuss the experiment toolbox to generate the TN state in the trapped-ion platform. In Fig. 12(a), we give the basic idea of the proposed scheme. The input phonon state (i.e., vacuum product state $|0\cdots0\rangle$) is sent into the phonon circuit, which consists of the two-mode (rank-4 tensor) operations and generates a rough but complex entanglement structure. Then the quantum information is transferred into qubits, and local qubits operations are done for improving the local details of the output TN states. Finally, the classical computer is used for the optimization of variational parameters (for the two-mode operations and two-qubit operations). In the following discussion, we consider the two-mode operations between the transverse collective modes [55,65] instead of the local modes [60–64], which provides the flexibility to couple different pairs of the phonon modes.

We briefly outline the basic idea for the proposed experiment setting here. In Sec. III A, we discuss in detail how to implement the two-mode operations; in Sec III B we discuss how to implement the quantum information transfer between the phonon mode and the qubit, after which one can apply the single- and two-qubit gate. The high optical access ion trap system [71] developed recently gives us the ability for addressing and manipulating ions individually, and also gives us the flexibility for the two-mode operations. The two Raman beams propagating towards the ion from opposite directions, which gives the photon motional kick $\Delta k$, can be used to drive the phonon sideband operations for both $x$ or $y$ modes (two transverse mode directions). The flexibility for the two-mode operation can be viewed from two aspects.

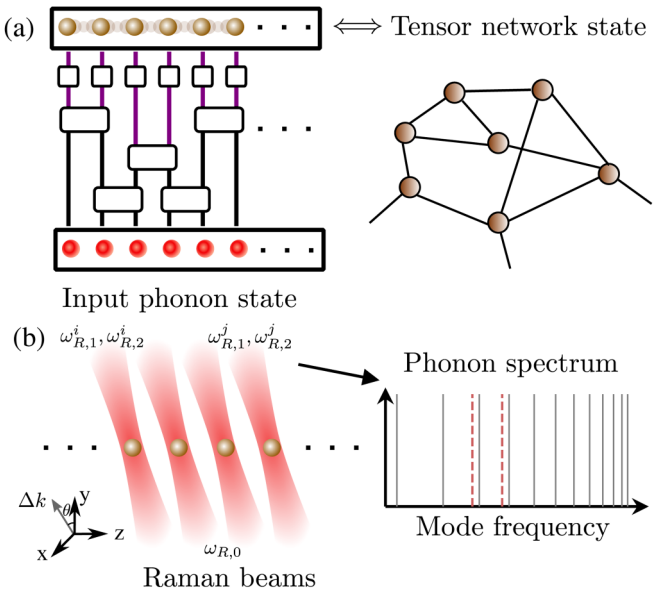


FIG. 12. (a) Schematic diagram of the proposed scheme. The input phonon state (vacuum product state $|0\cdots0\rangle$ for all the motional modes, shown as the red balls) is sent into the phonon circuit, and further transferred to the qubit entangled state (shown as the brown balls). Such state can be mapped to the highly entangled TN states, i.e., the MPS and the PEPS on the square lattice (detailed in Sec. II). The phonon circuit consists of the CMR (blue square) and the TMS (orange oval) operations. The circuit parameters are optimized on the classical computer. (b) Basic schematic diagram of the experimental proposal. The photon momentum $\Delta k$ is given by the momentum difference between Raman beams. The global beam has the frequency of $\omega_{R,0}$ while the individual addressing beams have frequency components $\omega_{R,1}$ and $\omega_{R,2}$. Also the laser intensity and the phase between the global beam and individual addressing beams are the variable parameters. The frequency difference between Raman beams is used to address phonon mode pairs for the two-mode operation. The detailed toolboxes for the operations and measurement schemes are shown in Figs. 13 and 14.

(1) High *connectivity* for the two-mode operations. We can implement two-mode operations with the $i$th ion qubit state as the auxiliary and carefully design Raman beams on it. As shown in Fig. 12(b), one of the Raman beams has the frequency $\omega_{R,0}$, which are the same for all ions. Another Raman beam contains two frequency components $\omega^i_{R,1}$ and $\omega^i_{R,2}$ and the corresponding phases $\phi^i_1$ and $\phi^i_2$. One can tune $\omega^i_{R,1}$ and $\omega^i_{R,2}$ on the $i$th ion to address the two-mode pairs in the phonon spectrum while having little effect on other modes. Different from the couplings between qubits, the couplings between collective modes are more flexible, for example, not limited by the position of ions.

(2) High *parallelism* for the two-mode operations. As we mentioned above, the Raman beam pairs on every ion can be tuned individually, also shown in Fig. 12(b). Assume we want the phonon circuit to have $N$ phonon modes as input, then for each layer of two-mode operations in the scheme the Raman beams can be applied to $N/2$ ions simultaneously with the desired frequencies $\omega^i_{R,1}$ and $\omega^i_{R,2}$ and phases $\phi^i_1$ and $\phi^i_2$. The qubit degree of freedom of ions is used as the auxiliary to couple the two modes, and all the two-mode operations can be done simultaneously and independently. Such parallelism for the two-mode operation shortens the circuit depth and is beneficial for suppressing error propagating.

It is worth discussing the technical advantages of using phonon operations (or hybrid with spin) instead of only the qubit operations for the building of the entanglement. For implementing a gate between two ion qubits, one needs phase-locking Raman beam pairs on two ions, while for the two-mode operations discussed below one only needs the Raman beam pair on a single ion to couple two phonon modes, and thus fewer Raman beams are required and less crosstalk occurs in principle. For example, $N$ Raman beam pairs are required to couple $N$ ions in pairs while $N/2$ Raman beam pairs are required to couple $N$ phonon modes in pairs (for a single layer). In addition, the two-mode operations can be applied to arbitrary phonon pairs, while the two-qubit operations are limited by the power-law decay for the coupling strength. In one word, the parallelism and connectivity of phonon modes are much better than the qubits. Besides, since the dimension of the Fock space is larger than the qubit Hilbert space, it is easier to generate a highly entangled state by the phonon modes. However, as discussed above, because of the lack of free parameters of the phonon operators, we need to utilize the abundant free parameters of the two-qubit gates to supply more free parameters and refine the local details of the generated TN states.

### A. Operations on phonon modes

Considering a chain with $N$ ions in a harmonic linear ion trap along the $z$ direction, the dimensionless equilibrium position of each ion $u_n \equiv z^{(0)}_n / \sqrt[3]{\frac{e^2}{4\pi\epsilon_0 M\nu_0^2}}$ can be calculated from the $N$ coupled algebraic equations $u_i - \sum_{j=1}^{i-1} 1/(u_j-u_i)^2 + \sum_{i=j+1}^{N} 1/(u_j-u_i)^2 = 0$, where $M$ is the mass of each ion, $e$ is the electron charge, $\epsilon_0$ is the permittivity of vacuum, and $\omega_0$ is the ion trap frequency (angular frequency). The interaction matrix of the transverse phonon modes is given below [45,70,82–84]:

$$A^{x(y)}_{ij} = \begin{cases} (\beta^{x(y)})^2 - \sum_{k\neq j}^{N} 1/|u_j-u_k|^3 & (i=j) \\ 1/|u_j-u_i|^3 & (i\neq j) \end{cases} \tag{9}$$

where $\beta^{x(y)} = \omega^{x(y)}/\omega_0$. By diagonalizing the matrix with $\mathbf{A}^{x(y)}\cdot\mathbf{b}^{x(y)}_m = \lambda^{x(y)}_m \mathbf{b}^{x(y)}_m$, we can obtain the eigenfrequencies $\omega^{x(y)}_m = \sqrt{\lambda^{x(y)}_m}\omega_0$ and the eigenvectors $\mathbf{b}^{x(y)}_m$ of the $m$th motional mode along the $x$ ($y$) axis. Then we can define the Lamb-Dicke parameters which describe the coupling between the laser beams and ion motions:

$$\begin{aligned} \eta^x_{im} &= \cos\theta(\mathbf{b}^x_m)_i \Delta k \sqrt{\frac{\hbar}{2m\omega^x_m}}, \\ \eta^y_{jn} &= \sin\theta(\mathbf{b}^y_n)_j \Delta k \sqrt{\frac{\hbar}{2m\omega^y_m}} \end{aligned} \tag{10}$$

where $\theta$ is the angle between $\Delta k$ and the $x$ axis. $\eta^{x(y)}_{im}$ above describes the coupling between the $i$th ion and $m$th motional mode. To simplify the symbol, below we ignore the direction

index $x$ and $y$ and only consider the mode index $m$, which can take the value from 1 to $2N$.

The Hamiltonian of the system with $N$ ions and the two Raman beams discussed above can be written as [48,64,70,84,85]

$$H = \sum_{i=1}^{N} \frac{\hbar\omega_{\mathrm{HPF}}}{2}\sigma_z^i + \sum_{m=1}^{2N} \hbar\omega_m \left(a_m^\dagger a_m + \frac{1}{2}\right) + \sum_{i=1}^{N}\sum_{j=1,2} \frac{\hbar\Omega_i}{2}\sigma_x^i [e^{i(\omega_j^i t - \Delta\vec{k}\cdot\vec{r} + \phi_j^i)} + e^{-i(\omega_j^i t - \Delta\vec{k}\cdot\vec{r} + \phi_j^i)}], \tag{11}$$

where $\omega_j^i = \omega_{R,0} - \omega_{R,j}^i$ are the effective laser frequencies for the Raman beams on the $i$th ion, $\sigma_z$ is the Pauli matrix, $\Delta\vec{k}\cdot\vec{r} = \Delta k_x x + \Delta k_y y$, $\Omega_i$ is the effective Rabi frequency on the $i$th ion, and $\phi_j^i$ are the phases for the $j$th frequency component on the $i$th ion. Actually, we can control at most $2N$ transverse motional modes at the same time if all $\Omega_i \neq 0$. However, for the quantum information transfer between the phonon mode and qubit in Sec. III B, we want to encode the multiphonon state back to the qubit levels, so at most $N$ phonon modes are used and corresponding Raman beams on $N/2$ ions. We further define the detuning as $\delta_j^i = \omega_j^i - \omega_{\mathrm{HPF}}$. In the interaction picture with $H_0 = \sum \frac{\hbar\omega_{\mathrm{HPF}}}{2}\sigma_z^i + \sum \hbar\omega_m(a_m^\dagger a_m + \frac{1}{2})$ and under Lamb-Dicke approximation $[\eta_{im}^2(2\langle n\rangle + 1) \ll 1]$, the interaction Hamiltonian is shown below:

$$H_{\mathrm{int}} = \sum_{i=1}^{N}\sum_{j=1,2} \frac{\hbar\Omega_i}{2} e^{-i\delta_j^i t} e^{i\phi_j^i}\sigma_+ \times [1 + \sum_m i\eta_{i,m}(a_m e^{-i\omega_m t} + a_m^\dagger e^{i\omega_m t})] + \mathrm{H.c.} \tag{12}$$

Based on the Hamiltonian above, we will discuss how to realize the basic phonon operations in the experiment with tunable $\delta_j^i$ and $\phi_j^i$ on the $i$th ion. In the following, we focus on the Raman beam pair on a single ion, i.e., the $i$th ion, and similarly for the Raman beams on other ions and motional modes, and ignore the index $i$ for the ion for simplification. We will give the detailed derivation in the Appendix, following [86] for the effective Hamiltonian theory.

In the following, we will discuss how to realize the two-mode operation in the phonon space [55,60–62,64,65,87], which is the core to generate the TN state in the ion trap. As mentioned in Eq. (10), the momentum kick $\Delta k$ overlaps with the collective modes in both the $x$ and $y$ axis, given by the nonzero Lamb-Dicke parameter $\eta$, which describes the coupling between the laser wave vector and motional modes. This system provides two-mode operations with high connectivity, for one can choose the detuning $w_j^i$ between the Raman beam pairs to address motional mode pairs. Also, these operations can be done in parallel and not limited by the ion separation. One can choose the $i$th ion coupled to $m$th and $n$th motional modes, which makes $\eta_{i,m}\eta_{i,n}$ larger, thus shortening the operation time in each layer. We give the operations and tunable parameters below [55,65], while leaving the detailed deviation for the Appendix.

The first kind of operation is the CMR operation, which guarantees the particle number and parity conservation in the Fock space. As shown in Fig. 13(a) with $\delta_1^i = -\omega_1 - \delta_R$ and $\delta_2^i = -\omega_2 - \delta_R$, here $\omega_1$ and $\omega_2$ are the frequencies for the modes we want to operate. With such pulse, the two-mode operation on modes 1 and mode 2 is given as

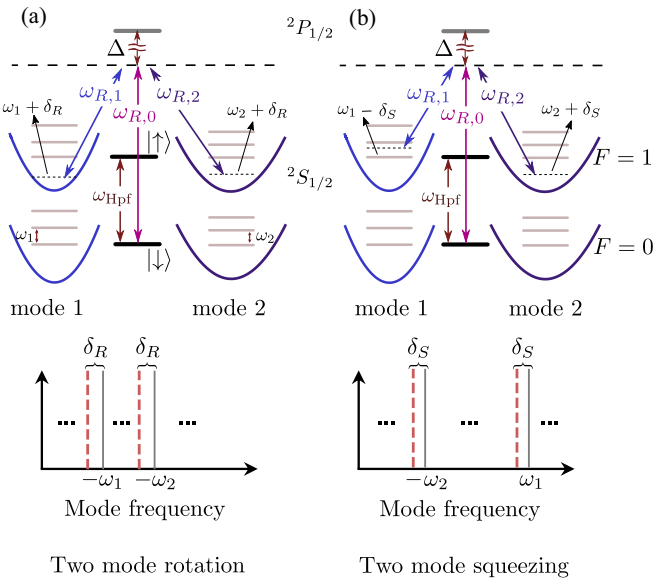


FIG. 13. Trapped-ion realization of the two-mode operations. Here we take $^{171}\mathrm{Yb}^+$ as an example and adapt the methods from [55,65]. The system has the qubit level encoded in the $^2S_{1/2}$ hyperfine level: $|\downarrow\rangle := |F = 0, m_F = 0\rangle$ and $|\uparrow\rangle := |F = 1, m_F = 0\rangle$. Motional degree of freedom mode 1 and mode 2 are coupled to the system qubit with the frequency $\omega_1$ (blue curve) and $\omega_2$ (purple curve). The lower one corresponds to the $|\downarrow\rangle$ phonon state and the upper one corresponds to the $|\uparrow\rangle$ phonon state. The (a) CMR operation $R(\theta, \phi)$ and (b) TMS operation $S(\gamma, \varphi)$ are implemented via controlling the frequencies $\omega_{R,0}$, $\omega_{R,1}$, $\omega_{R,2}$ and phase $\phi_1$, $\phi_2$. The lower row denotes the phonon spectrum and the required detuning for the corresponding mode operation.

$$R(\theta,\phi) = \exp\left\{-i\frac{\theta}{2}(a_1^\dagger a_2 e^{i\phi} + a_1 a_2^\dagger e^{-i\phi})\sigma_z\right\},$$
$$U_{\mathrm{CMR}}(\theta,\phi) = \exp\left\{-i\frac{\theta}{2}(e^{i\phi}a_1^\dagger a_2 + e^{-i\phi}a_1 a_2^\dagger)\right\}, \tag{13}$$

where $\eta_1$ and $\eta_2$ are the Lamb-Dicke parameters for mode 1 and mode 2, $\theta = t\eta_1\eta_2\Omega^2/8\delta_R$, and $\phi = \phi_2 - \phi_1$. With the qubit state prepared in the $(\sigma_z)$ eigenstate, the CMR operation $U_{\mathrm{CMR}}$ can be implemented.

The second kind of operation is the TMS operation, which only guarantees parity conservation in the Fock space. As shown in Fig. 13(b) with $\delta_1 = \omega_1 - \delta_S$ and $\delta_2 = -\omega_2 - \delta_S$, $\omega_1$ and $\omega_2$ are still the frequencies for the modes we want to operate. With such pulse, the two-mode operation on modes 1 and mode 2 is given as

$$S(\gamma,\psi) = \exp\left\{-i\frac{\gamma}{2}(a_1^\dagger a_2^\dagger e^{i\psi} + a_1^\dagger a_2^\dagger e^{-i\psi})\sigma_z\right\},$$
$$U_{\mathrm{TMS}}(\gamma,\psi) = \exp\left\{-i\frac{\gamma}{2}(e^{i\psi}a_1^\dagger a_2^\dagger + e^{-i\psi}a_1^\dagger a_2^\dagger)\right\} \tag{14}$$

where $\eta_1$ and $\eta_2$ are the Lamb-Dicke parameters for mode 1 and mode 2, $\gamma = t\eta_1\eta_2\Omega^2/8\delta_S$, and $\psi = \phi_2 - \phi_1$. With the

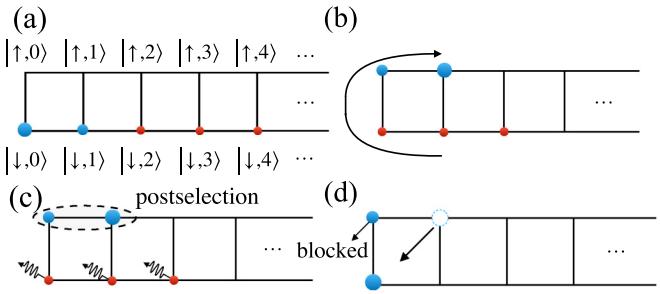


FIG. 14. Details on the phonon-qubit hybrid technology. The goal is to coherently transfer the $|0\rangle$ ($|1\rangle$) phonon state to the $|\downarrow\rangle$ ($|\uparrow\rangle$) state, while other parts are postselected. (a) Initial state we consider (output from the phonon circuit), where phonon and qubit degrees of freedom get decoupled. Blue circles denote the state we want to transfer and red circles denote the state we want to remove. (b) "Rolled" operation $U_R$ for the phonon and qubit state, where $n \leqslant 1$ phonon states are "rolled" to the $|\uparrow\rangle$ qubit state and $n > 1$ phonon states shift left by 2. (c) All the phonon states coupled with the $|\downarrow\rangle$ qubit state are removed (with the laser pulse connecting $|\downarrow\rangle$ and other excited states). (d) Blue sideband pulse from $|\uparrow, 1\rangle$ to $|\downarrow, 0\rangle$. Notice $|\uparrow, 0\rangle$ cannot be driven during this step. After the pulse sequence above, we transfer the correlation between phonon modes to the ion qubits.

qubit state prepared in the eigenstate of $\sigma_z$, CMR operation $U_{\mathrm{CMR}}$ can be implemented.

### B. Transfer from multiphonon state to qubit entangled state

In this section, we will discuss how to transfer the correlation between phonon modes to the ion qubits degree of freedom as required for further qubit operations. As we have shown above, we send the initial product state to the phonon circuit composed of the TMS and the CMR, and get a $N$ phonon modes state which gets decoupled with qubit states:

$$|\psi\rangle_{\mathrm{out}} = \sum_{i_1,\cdots,i_N=0}^{\infty} c_{i_1,\cdots,i_N}|\downarrow_1,\cdots,\downarrow_N, i_1,\cdots,i_N\rangle. \quad (15)$$

Next, via the phonon-qubit hybrid technology, we transfer the partial quantum information in the phonon number subspace $\{|0\rangle, |1\rangle\}$ of each mode to each ion qubit state $\{|\downarrow\rangle, |\uparrow\rangle\}$. Then with the $N$ qubits entangled state (from the $N$ phonon modes entangled state) at hand, we can perform the qubit operation on it to improve the expressive power of the scheme and do standard qubit measurement to estimate the expected value of observables.

Now we give the details of the whole process shown in Fig. 14.

(1) As shown in Fig. 14(b), first we perform the "rolled" operation mentioned in [65], which gives

$$U_R = |1,\uparrow\rangle\langle 0,\downarrow| + |0,\uparrow\rangle\langle 1,\downarrow| + \sum_{n>1}|n-2,\downarrow\rangle\langle n,\downarrow|. \quad (16)$$

After this operation, $n \leqslant 1$ phonon states get rolled to the $|\uparrow\rangle$ state, while $n > 1$ phonon states have their phonon number decreased by two. Also, $U_R$ can be performed on each individual qubit, and we can address a single motional mode with the selected detuning of the driving pulse close to the mode frequency. With these operations, the phonon and qubit state get coupled as

$$|\psi\rangle_1 = \sum_{i_1,\cdots,i_n=0}^{1} c_{i_1,\cdots,i_n}|\uparrow_1, 1-i_1\rangle \otimes \cdots \otimes |\uparrow_n, 1-i_n\rangle + \text{others}, \quad (17)$$

where "others" contains the states with at least one qubit in the $|\downarrow\rangle$ state.

(2) As shown in Fig. 14(c), we can use the laser pulse to drive the $|\downarrow\rangle$ to ancillary state $|e\rangle$, which is away from the qubit state manifold. The driving left the quantum state similar to Eq. (17): if the phonon number for the $m$th motional mode $i_m \leqslant 1$, then the corresponding $m$th ion is in $|\uparrow\rangle$; if the $m$th mode $i_m > 1$, then the corresponding $m$th ion is in $|e\rangle$. In other words, "others" contains the states with at least one qubit in the $|e\rangle$ state.

(3) Postselection to the space where all the qubits are in the $|\uparrow\rangle$ state can be done by measuring the qubit state of all the ions on the $|\uparrow\rangle$ state. When there exist ions in the $|e\rangle$ state, the quantum states get discorded. The quantum state after postselection can be written as

$$|\psi\rangle_2 = \frac{1}{\mathcal{N}} \sum_{i_1,\cdots,i_N=0,1} c_{i_1,\cdots,i_N}|\uparrow_1, 1-i_1\rangle \otimes \cdots \otimes |\uparrow_N, 1-i_N\rangle, \quad (18)$$

where $\mathcal{N}$ is the normalized factor. The postselection probability is high since the TMS operation makes the part in which the phonon number on each site is less than 2 dominant.

(4) Finally, as shown in Fig. 14(d), we can perform the regular blue sideband transition between $|\uparrow, n+1\rangle \leftrightarrow |\downarrow, n\rangle$. Notice that such transition is blocked for the $|\uparrow, 0\rangle$ state, and $n > 1$ phonon states are absent; we do not worry about the inhomogeneous driving in the sideband transition [88,89]. Thus the final quantum state we obtain is

$$|\psi\rangle_3 = \frac{1}{\mathcal{N}} \sum_{s_1,\cdots,s_N=\downarrow,\uparrow} c_{s_1,\cdots,s_N}|s_1,\cdots,s_N\rangle \otimes |i_1,\cdots,i_N = 0\rangle, \quad (19)$$

where the motional degrees of freedom are $|n_m = 0\rangle$ for all the modes, and the information is transferred to the qubit state. With the phonon-qubit hybrid technology, we can improve the expressive power by further performing the qubit operation.

## IV. NUMERICAL SIMULATION

To benchmark the validity of the ideas mentioned before, we simulate the ground state of the 1D Heisenberg model $H_{\mathrm{Heisenberg}} = J\sum_i(\sigma_x^i\sigma_x^{i+1} + \sigma_y^i\sigma_y^{i+1} + \sigma_z^i\sigma_z^{i+1})$ and 1D transverse-field Ising model near the critical point $H_{\mathrm{Ising}} = J\sum_i(\sigma_x^i\sigma_x^{i+1} + \sigma_z^i)$ with different types of MERA *Ansatz*. In order to compare the experimental results near the future, we set the length of the 1D chain to be 5 and 11.

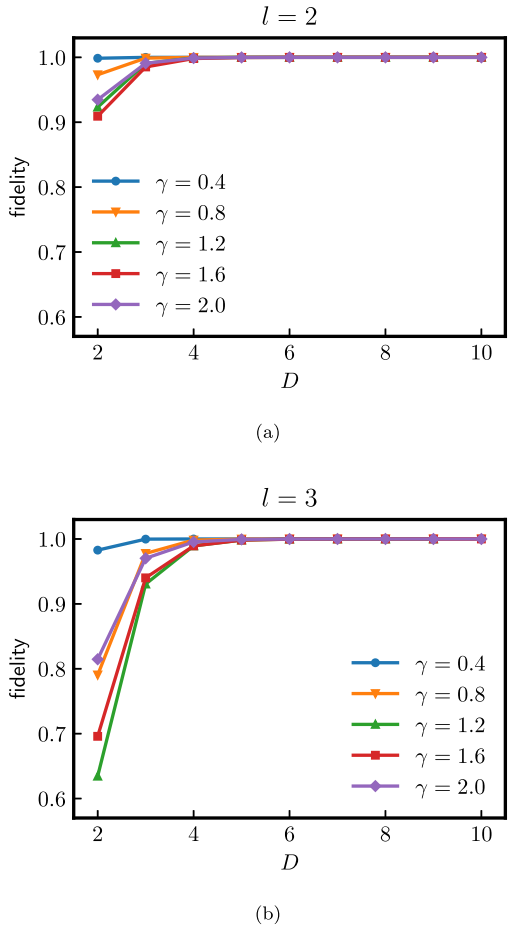


FIG. 15. The fidelity between the states with the phonon number cut $D$ and $D = 20$ after postselecting into $\{|0\rangle, |1\rangle\}$ subspace in the different layers of MERA on the 1D lattice with the same parameters at each site. For all results, we set the rotation parameter and phase parameters of the CMR $\theta = 0, \phi = 0$ [in Eq. (13)], and the phase parameters of the TMS $\psi = 0$ [in Eq. (14)]. The blue round dot is the result with squeezing parameter $\gamma = 0.4$ [in Eq. (14)], the orange inverted triangle dot is for $\gamma = 0.8$, the green triangle dot is for $\gamma = 1.2$, the red square dot is for $\gamma = 1.6$, and the purple diamond dot is for $\gamma = 2.0$. (a) The results for two-layer MERA on the 1D lattice with different squeezing parameters. (b) The results for three-layer MERA on the 1D lattice with different squeezing parameters.

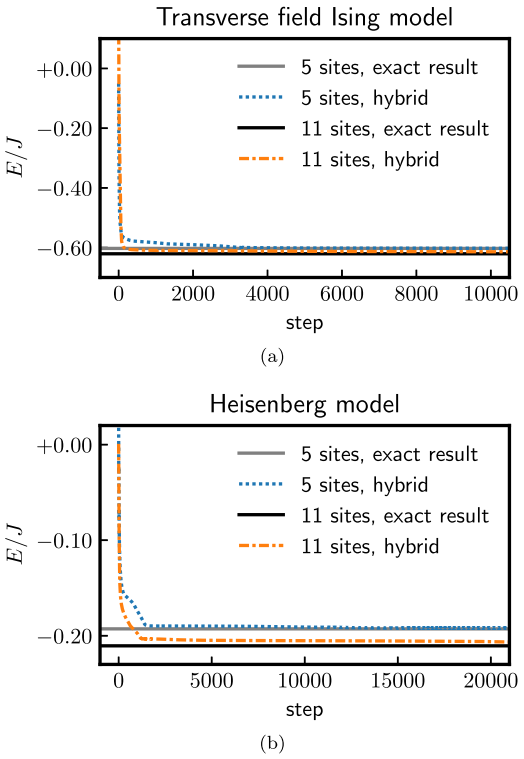


FIG. 16. The optimized energy results calculated from the MERA *Ansatz*. The vertical axis is the energy per site, and the horizontal axis is the iteration step of the gradient descent method. For both of the figures, the gray (black) horizontal line is the theoretical result given by the exact diagonalization method, and the blue dotted (orange dash-dotted) line is the result obtained from the MERA *Ansatz*. (a) The results for the 5- and 11-site transverse-field Ising model near the critical point. (b) The results for the 5- and 11-site Heisenberg model.

In our simulation, all the input states (the green legs in Fig. 10) are set to vacuum state ($|0\rangle$), and the numerical calculation is based on the TNSPACKAGE [90].

In order to compare our simulation results with the experimental results, we need to consider the Fock states with multiple phonon numbers (corresponding to the tensor with large $D$). Since the amplitude of the Fock state $|n\rangle$ decays with $n$ because of the TMS operation, thus we can simulate the experimental results with the MERA *Ansatz* reliably with suitable truncation of the phonon number. In Fig. 15, we test the relation between the exact results and the result with the truncation of the phonon $D_{\text{cut}}$ with two- and three-layer MERA *Ansätze*, where the exact results are obtained by truncating the phonon number to 20, which is big enough. Actually, we can find that the fidelity between the MERA with truncation dimension $D_{\text{cut}}$ and the exact result is saturated when $D_{\text{cut}}$ is bigger than 5. With this result, we set the truncation parameter $D_{\text{cut}}$ to be 6 in our simulation, which is enough to guarantee its reliability.

Then, we numerically simulate the energy of the ground states of the 11-site (5-site) 1D transverse-field Ising model near the critical point and Heisenberg model with the MERA *Ansatz*. In Fig. 16, the ground energy obtained in our simulation (blue dotted line and orange dashdotted line) is very close to the exact value (the relative errors, i.e., $\frac{E_{\text{num}}-E_{\text{th}}}{E_{\text{th}}}$, are as small as 0.003 and 0.4% for 5- and 11-site 1D transverse-field Ising models separately, and as small as 0.5 and 1% for 5- and 11-site 1D Heisenberg models separately). It is clear that the TN states generated by the phonon-qubit TN states generation scheme can well represent the ground state of the 1D transverse-field Ising model near the critical point and Heisenberg model. If we add more operations into the unitary element $U(\boldsymbol{\Theta})$ to introduce more free parameters, the results can be further improved.

By the way, the results with the MERA *Ansatz* with only phonon operation are far away from the exact result, which indicates that the lack of free parameters of the phonon operations is the fatal flaw.

## V. SUMMARY

In this paper, we propose a scheme to generate the TN state in the trapped-ion platform by combining the phonon modes and qubits. Due to the full connectivity of the phonon operation, the complex TN states with rough entanglement structure can be generated programmably. We take the MERA on the 1D lattice and the PEPS on the kagome lattice as examples, in addition to the already generated MPS and PEPS on the square lattice by other schemes. The parallelism of the phonon operations makes the depth of the generation circuit very shallow, which supplies additional robustness against the noise. With the phonon-qubit hybrid technology, we introduce the local qubit operations into our scheme. Due to the abundant free parameters of the qubit operations, we refine the local details of the generated TN states, and the expressive power of the generated TN state is dramatically improved. As shown in numerical results, the TN states generated by our scheme can be used to be a variational ground state of a many-body system, which may offer a way to demonstrate quantum advantage by replacing the contraction of tensors. Our numerical simulation supports all of our ideas. Last but not least, recent experimental progress towards generation of the phonon network [56] enhances the feasibility of our scheme, and the analysis in the paper on scaling up to more phonon modes also applies to our system.

## ACKNOWLEDGMENTS

This work was supported by the National Natural Science Foundation of China (Grant No. 11874343), the Key Research Program of Frontier Sciences, Chinese Academy of Sciences (CAS) (Grant No. QYZDY-SSW-SLH003), Science Foundation of the CAS (Grant No. ZDRW-XH-2019-1).

S.-J.T. and H.-Q.Z. contributed equally to this work.

## APPENDIX: PHONON MODE OPERATION DERIVATION

In this part, we will derive Eqs. (13) and (14) in the main text, following [86]. Basically, in the interaction picture, the time-dependent Hamiltonian has the form

$$\hat{H}_I(t) = \sum_{n=1}^{N} \hat{h}_n \exp(-i\omega_n t) + \hat{h}_n^\dagger \exp(i\omega_n t) \tag{A1}$$

and then we have the effective Hamiltonian to describe the system as

$$\hat{H}_{\text{eff}}(t) = \sum_{m,n=1}^{N} \frac{1}{\hbar\bar{\omega}_{mn}} [\hat{h}_m^\dagger, \hat{h}_n] \exp(i[\omega_m - \omega_n]t) \tag{A2}$$

with

$$\frac{1}{\bar{\omega}_{mn}} = \frac{1}{2}\left(\frac{1}{\omega_m} + \frac{1}{\omega_n}\right). \tag{A3}$$

In the case for the CMR operation, we have

$$\begin{aligned} h_1 &= -i\eta_1 \frac{\hbar\Omega}{2} e^{-i\phi_1} \sigma_- a_1^\dagger, \\ h_2 &= -i\eta_2 \frac{\hbar\Omega}{2} e^{-i\phi_2} \sigma_- a_2^\dagger \end{aligned} \tag{A4}$$

with $\omega_1 = \omega_2 = \delta_R$ and effective Hamiltonian

$$\hat{H}_{\text{eff}} = \frac{\hbar\Omega^2\eta_1\eta_2}{4\delta_R}\left(a_1^\dagger a_2 e^{i\phi_B} + a_1 a_2^\dagger e^{-i\phi_B}\right)\sigma_z. \tag{A5}$$

Similarly, for the TMS operation we have

$$\begin{aligned} h_1 &= -i\eta_m \frac{\hbar\Omega}{2} e^{-i\phi_1} \sigma_- a_1, \\ h_2 &= -i\eta_m \frac{\hbar\Omega}{2} e^{-i\phi_2} \sigma_- a_2^\dagger, \end{aligned} \tag{A6}$$

and effective Hamiltonian

$$\hat{H}_{\text{eff}} = \frac{\hbar\Omega^2\eta_1\eta_2}{4\delta_S}\left(a_1^\dagger a_2^\dagger e^{i\phi_B} + a_1 a_2 e^{-i\phi_B}\right)\sigma_z. \tag{A7}$$

[1] S. Sachdev, *Quantum Phase Transitions* (Cambridge University, Cambridge, England, 2011).

[2] H. J. Liao, Z. Y. Xie, J. Chen, Z. Y. Liu, H. D. Xie, R. Z. Huang, B. Normand, and T. Xiang, Gapless Spin-Liquid Ground State in the S = 1/2 Kagome Antiferromagnet, Phys. Rev. Lett. **118**, 137202 (2017).

[3] P. A. Lee, N. Nagaosa, and X.-G. Wen, Doping a Mott insulator: Physics of high-temperature superconductivity, Rev. Mod. Phys. **78**, 17 (2006).

[4] W. M. C. Foulkes, L. Mitas, R. J. Needs, and G. Rajagopal, Quantum monte carlo simulations of solids, Rev. Mod. Phys. **73**, 33 (2001).

[5] F. Becca and S. Sorella, *Quantum Monte Carlo Approaches for Correlated Systems* (Cambridge University, Cambridge, England, 2017).

[6] J. Lowe, *Quantum Chemistry* (Academic, London, 1993).

[7] M. C. Gutzwiller, Effect of Correlation on the Ferromagnetism of Transition Metals, Phys. Rev. Lett. **10**, 159 (1963).

[8] D. S. Rokhsar and B. G. Kotliar, Gutzwiller projection for bosons, Phys. Rev. B **44**, 10328 (1991).

[9] R. Orús, A practical introduction to tensor networks: Matrix product states and projected entangled pair states, Ann. Phys. (NY) **349**, 117 (2014).

[10] R. Orús, Tensor networks for complex quantum systems, Nat. Rev. Phys. **1**, 538 (2019).

[11] M. B. Hastings, An area law for one-dimensional quantum systems, J. Stat. Mech.: Theory Exp. (2007) P08024.

[12] N. Schuch, M. M. Wolf, F. Verstraete, and J. I. Cirac, Entropy Scaling and Simulability by Matrix Product States, Phys. Rev. Lett. **100**, 030504 (2008).

[13] Z.-C. Gu, M. Levin, and X.-G. Wen, Tensor-entanglement renormalization group approach as a unified method for symmetry breaking and topological phase transitions, Phys. Rev. B **78**, 205116 (2008).

[14] J. I. Cirac, D. Poilblanc, N. Schuch, and F. Verstraete, Entanglement spectrum and boundary theories with projected entangled-pair states, Phys. Rev. B **83**, 245134 (2011).
[15] J. I. Cirac, D. Pérez-García, N. Schuch, and F. Verstraete, Matrix product density operators: Renormalization fixed points and boundary theories, Ann. Phys. (NY) **378**, 100 (2017).
[16] F. Verstraete and J. I. Cirac, Renormalization algorithms for quantum-many body systems in two and higher dimensions, arXiv:cond-mat/0407066.
[17] F. Verstraete, V. Murg, and J. I. Cirac, Matrix product states, Projected entangled pair states, and variational renormalization group methods for quantum spin systems, Adv. Phys. **57**, 143 (2008).
[18] W.-Y. Liu, S.-J. Dong, Y.-J. Han, G.-C. Guo, and L. He, Gradient optimization of finite projected entangled pair states, Phys. Rev. B **95**, 195154 (2017).
[19] M. M. Wolf, Violation of the Entropic Area Law for Fermions, Phys. Rev. Lett. **96**, 010404 (2006).
[20] C. Schön, E. Solano, F. Verstraete, J. I. Cirac, and M. M. Wolf, Sequential Generation of Entangled Multiqubit States, Phys. Rev. Lett. **95**, 110503 (2005).
[21] C. Schön, K. Hammerer, M. M. Wolf, J. I. Cirac, and E. Solano, Sequential generation of matrix-product states in cavity QED, Phys. Rev. A **75**, 032311 (2007).
[22] S. Xu and S. Fan, Generate tensor network state by sequential single-photon scattering in waveguide QED systems, APL Photonics **3**, 116102 (2018).
[23] Z.-Y. Wei, D. Malz, A. González-Tudela, and J. I. Cirac, Generation of photonic matrix product states with Rydberg atomic arrays, Phys. Rev. Research **3**, 023021 (2021).
[24] Z.-Y. Wei, J. I. Cirac, and D. Malz, Generation of photonic tensor network states with circuit qed, Phys. Rev. A **105**, 022611 (2022).
[25] H. Pichler, S. Choi, P. Zoller, and M. D. Lukin, Universal photonic quantum computation via time-delayed feedback, Proc. Natl. Acad. Sci. USA **114**, 11362 (2017).
[26] I. Dhand, M. Engelkemeier, L. Sansoni, S. Barkhofen, C. Silberhorn, and M. B. Plenio, Proposal for Quantum Simulation via All-Optically-Generated Tensor Network States, Phys. Rev. Lett. **120**, 130501 (2018).
[27] M. Lubasch, A. A. Valido, J. J. Renema, W. S. Kolthammer, D. Jaksch, M. S. Kim, I. Walmsley, and R. García-Patrón, Tensor network states in time-bin quantum optics, Phys. Rev. A **97**, 062304 (2018).
[28] M. Foss-Feig, D. Hayes, J. M. Dreiling, C. Figgatt, J. P. Gaebler, S. A. Moses, J. M. Pino, and A. C. Potter, Holographic quantum algorithms for simulating correlated spin systems, Phys. Rev. Research **3**, 033002 (2021).
[29] I. MacCormack, A. Galda, and A. L. Lyon, Simulating large PEPS tensor networks on small quantum devices, arXiv:2110.00507.
[30] M. Foss-Feig, S. Ragole, A. Potter, J. Dreiling, C. Figgatt, J. Gaebler, A. Hall, S. Moses, J. Pino, B. Spaun, B. Neyenhuis, and D. Hayes, Entanglement from Tensor Networks on a Trapped-Ion Quantum Computer, Phys. Rev. Lett. **128**, 150504 (2022).
[31] C. Eichler, J. Mlynek, J. Butscher, P. Kurpiers, K. Hammerer, T. J. Osborne, and A. Wallraff, Exploring Interacting Quantum Many-Body Systems by Experimentally Creating Continuous Matrix Product States in Superconducting Circuits, Phys. Rev. X **5**, 041044 (2015).
[32] E. Chertkov, J. Bohnet, D. Francois, J. Gaebler, D. Gresh, A. Hankin, K. Lee, R. Tobey, D. Hayes, B. Neyenhuis, R. Stutz, A. C. Potter, and M. Foss-Feig, Holographic dynamics simulations with a trapped ion quantum computer, arXiv:2105.09324.
[33] Z.-Y. Wei, D. Malz, and J. I. Cirac, Sequential Generation of Projected Entangled-Pair States, Phys. Rev. Lett. **128**, 010607 (2022).
[34] G. Vidal, Class of Quantum Many-Body States That Can Be Efficiently Simulated, Phys. Rev. Lett. **101**, 110501 (2008).
[35] G. Evenbly and G. Vidal, Tensor network states and geometry, J. Stat. Phys. **145**, 891 (2011).
[36] B. Swingle, Entanglement renormalization and holography, Phys. Rev. D **86**, 065007 (2012).
[37] N. Schuch, D. Poilblanc, J. I. Cirac, and D. Pérez-García, Resonating valence bond states in the peps formalism, Phys. Rev. B **86**, 115108 (2012).
[38] Z. Y. Xie, J. Chen, J. F. Yu, X. Kong, B. Normand, and T. Xiang, Tensor Renormalization of Quantum Many-Body Systems Using Projected Entangled Simplex States, Phys. Rev. X **4**, 011025 (2014).
[39] T. Picot, M. Ziegler, R. Orús, and D. Poilblanc, Spin-*s* kagome quantum antiferromagnets in a field with tensor networks, Phys. Rev. B **93**, 060407 (2016).
[40] J. I. Cirac and P. Zoller, Quantum Computations with Cold Trapped Ions, Phys. Rev. Lett. **74**, 4091 (1995).
[41] H. Häffner, C. F. Roos, and R. Blatt, Quantum computing with trapped ions, Phys. Rep. **469**, 155 (2008).
[42] J. M. Pino, J. M. Dreiling, C. Figgatt, J. P. Gaebler, S. A. Moses, M. S. Allman, C. H. Baldwin, M. Foss-Feig, D. Hayes, K. Mayer, C. Ryan-Anderson, and B. Neyenhuis, Demonstration of the trapped-ion quantum CCD computer architecture, Nature (London) **592**, 209 (2021).
[43] I. Pogorelov, T. Feldker, C. D. Marciniak, L. Postler, G. Jacob, O. Krieglsteiner, V. Podlesnic, M. Meth, V. Negnevitsky, M. Stadler, B. Höfer, C. Wächter, K. Lakhmanskiy, R. Blatt, P. Schindler, and T. Monz, Compact ion-trap quantum computing demonstrator, PRX Quantum **2**, 020343 (2021).
[44] K. Mølmer and A. Sørensen, Multiparticle Entanglement of Hot Trapped Ions, Phys. Rev. Lett. **82**, 1835 (1999).
[45] S.-L. Zhu, C. Monroe, and L.-M. Duan, Trapped Ion Quantum Computation with Transverse Phonon Modes, Phys. Rev. Lett. **97**, 050505 (2006).
[46] T. Choi, S. Debnath, T. A. Manning, C. Figgatt, Z.-X. Gong, L.-M. Duan, and C. Monroe, Optimal Quantum Control of Multimode Couplings between Trapped Ion Qubits for Scalable Entanglement, Phys. Rev. Lett. **112**, 190502 (2014).
[47] V. M. Schäfer, C. J. Ballance, K. Thirumalai, L. J. Stephenson, T. G. Ballance, A. M. Steane, and D. M. Lucas, Fast quantum logic gates with trapped-ion qubits, Nature (London) **555**, 75 (2018).
[48] Y. Lu, S. Zhang, K. Zhang, W. Chen, Y. Shen, J. Zhang, J.-N. Zhang, and K. Kim, Global entangling gates on arbitrary ion qubits, Nature (London) **572**, 363 (2019).
[49] Z. Davoudi, N. M. Linke, and G. Pagano, Toward simulating quantum field theories with controlled phonon-ion dynamics: A hybrid analog-digital approach, Phys. Rev. Research **3**, 043072 (2021).

[50] J. Casanova, L. Lamata, I. L. Egusquiza, R. Gerritsma, C. F. Roos, J. J. García-Ripoll, and E. Solano, Quantum Simulation of Quantum Field Theories in Trapped Ions, Phys. Rev. Lett. **107**, 260501 (2011).

[51] J. Casanova, A. Mezzacapo, L. Lamata, and E. Solano, Quantum Simulation of Interacting Fermion Lattice Models in Trapped Ions, Phys. Rev. Lett. **108**, 190502 (2012).

[52] A. Mezzacapo, J. Casanova, L. Lamata, and E. Solano, Digital Quantum Simulation of the Holstein Model in Trapped Ions, Phys. Rev. Lett. **109**, 200501 (2012).

[53] A. Macridin, P. Spentzouris, J. Amundson, and R. Harnik, Electron-Phonon Systems on a Universal Quantum Computer, Phys. Rev. Lett. **121**, 110504 (2018).

[54] J. Knörzer, T. Shi, E. Demler, and J. I. Cirac, Spin-Holstein Models in Trapped-Ion Systems, Phys. Rev. Lett. **128**, 120404 (2022).

[55] W. Chen, J. Gan, J.-N. Zhang, D. Matuskevich, and K. Kim, Quantum computation and simulation with vibrational modes of trapped ions, Chin. Phys. B **30**, 060311 (2021).

[56] W. Chen, Y. Lu, S. Zhang, K. Zhang, G. Huang, M. Qiao, X. Su, J. Zhang, J. Zhang, L. Banchi, M. S. Kim, and K. Kim, Scalable and programmable phononic network with trapped ions, arXiv:2207.06115 v1.

[57] D. Kienzler, H.-Y. Lo, B. Keitch, L. De Clercq, F. Leupold, F. Lindenfelser, M. Marinelli, V. Negnevitsky, and J. Home, Quantum harmonic oscillator state synthesis by reservoir engineering, Science **347**, 53 (2015).

[58] C. Flühmann, T. L. Nguyen, M. Marinelli, V. Negnevitsky, K. Mehta, and J. Home, Encoding a qubit in a trapped-ion mechanical oscillator, Nature (London) **566**, 513 (2019).

[59] B. de Neeve, T.-L. Nguyen, T. Behrle, and J. P. Home, Error correction of a logical grid state qubit by dissipative pumping, Nat. Phys. **18**, 296 (2022).

[60] K. Toyoda, Y. Matsuno, A. Noguchi, S. Haze, and S. Urabe, Experimental Realization of a Quantum Phase Transition of Polaritonic Excitations, Phys. Rev. Lett. **111**, 160501 (2013).

[61] K. Toyoda, R. Hiji, A. Noguchi, and S. Urabe, Hong-Ou-Mandel interference of two phonons in trapped ions, Nature (London) **527**, 74 (2015).

[62] M. Tamura, T. Mukaiyama, and K. Toyoda, Quantum Walks of a Phonon in Trapped Ions, Phys. Rev. Lett. **124**, 200501 (2020).

[63] C. Shen, Z. Zhang, and L.-M. Duan, Scalable Implementation of Boson Sampling with Trapped Ions, Phys. Rev. Lett. **112**, 050504 (2014).

[64] S. Debnath, N. M. Linke, S.-T. Wang, C. Figgatt, K. A. Landsman, L.-M. Duan, and C. Monroe, Observation of Hopping and Blockade of Bosons in a Trapped Ion Spin Chain, Phys. Rev. Lett. **120**, 073001 (2018).

[65] Y. Shen, Y. Lu, K. Zhang, J. Zhang, S. Zhang, J. Huh, and K. Kim, Quantum optical emulation of molecular vibronic spectroscopy using a trapped-ion device, Chem. Sci. **9**, 836 (2018).

[66] S. Ding, G. Maslennikov, R. Hablützel, and D. Matsukevich, Cross-Kerr Nonlinearity for Phonon Counting, Phys. Rev. Lett. **119**, 193602 (2017).

[67] S. Ding, G. Maslennikov, R. Hablützel, and D. Matsukevich, Quantum Simulation with a Trilinear Hamiltonian, Phys. Rev. Lett. **121**, 130502 (2018).

[68] G. Maslennikov, S. Ding, R. Hablützel, J. Gan, A. Roulet, S. Nimmrichter, J. Dai, V. Scarani, and D. Matsukevich, Quantum absorption refrigerator with trapped ions, Nat. Commun. **10**, 1 (2019).

[69] H. Gan, G. Maslennikov, K.-W. Tseng, C. Nguyen, and D. Matsukevich, Hybrid Quantum Computing with Conditional Beam Splitter Gate in Trapped Ion System, Phys. Rev. Lett. **124**, 170502 (2020).

[70] D. Leibfried, R. Blatt, C. Monroe, and D. Wineland, Quantum dynamics of single trapped ions, Rev. Mod. Phys. **75**, 281 (2003).

[71] R. He, J.-M. Cui, R.-R. Li, Z.-H. Qian, Y. Chen, M.-Z. Ai, Y.-F. Huang, C.-F. Li, and G.-C. Guo, An ion trap apparatus with high optical access in multiple directions, Rev. Sci. Instrum. **92**, 073201 (2021).

[72] F. Verstraete, D. Porras, and J. I. Cirac, Density Matrix Renormalization Group and Periodic Boundary Conditions: A Quantum Information Perspective, Phys. Rev. Lett. **93**, 227205 (2004).

[73] F. Verstraete, M. M. Wolf, D. Perez-Garcia, and J. I. Cirac, Criticality, the Area Law, and the Computational Power of Projected Entangled Pair States, Phys. Rev. Lett. **96**, 220601 (2006).

[74] G. Evenbly and G. Vidal, Algorithms for entanglement renormalization, Phys. Rev. B **79**, 144108 (2009).

[75] J. Maldacena, The large-N limit of superconformal field theories and supergravity, Int. J. Theor. Phys. **38**, 1113 (1999).

[76] V. E. Hubeny, The AdS/CFT correspondence, Class. Quantum Grav. **32**, 124010 (2015).

[77] U. Schollwöck, The density-matrix renormalization group in the age of matrix product states, Ann. Phys. (NY) **326**, 96 (2011).

[78] N. Schuch, M. M. Wolf, F. Verstraete, and J. I. Cirac, Computational Complexity of Projected Entangled Pair States, Phys. Rev. Lett. **98**, 140506 (2007).

[79] L. He, H. An, C. Yang, F. Wang, J. Chen, C. Wang, W. Liang, S. Dong, Q. Sun, W. Han, W. Liu, Y. Han, and W. Yao, PEPS $++$: Towards Extreme-Scale Simulations of Strongly Correlated Quantum Many-Particle Models on Sunway TaihuLight, IEEE Trans. Parallel Distrib. Syst. **29**, 2838 (2018).

[80] D. Porras and J. I. Cirac, Effective Quantum Spin Systems with Trapped Ions, Phys. Rev. Lett. **92**, 207901 (2004).

[81] K. Kim, M.-S. Chang, R. Islam, S. Korenblit, L.-M. Duan, and C. Monroe, Entanglement and Tunable Spin-Spin Couplings between Trapped Ions Using Multiple Transverse Modes, Phys. Rev. Lett. **103**, 120502 (2009).

[82] S.-L. Zhu, C. Monroe, and L.-M. Duan, Arbitrary-speed quantum gates within large ion crystals through minimum control of laser beams, Europhys. Lett. **73**, 485 (2006).

[83] P. H. Leung, K. A. Landsman, C. Figgatt, N. M. Linke, C. Monroe, and K. R. Brown, Robust 2-Qubit Gates in a Linear Ion Crystal Using a Frequency-Modulated Driving Force, Phys. Rev. Lett. **120**, 020501 (2018).

[84] C. Monroe, W. C. Campbell, L.-M. Duan, Z.-X. Gong, A. V. Gorshkov, P. W. Hess, R. Islam, K. Kim, N. M. Linke, G. Pagano, P. Richerme, C. Senko, and N. Y. Yao, Programmable quantum simulations of spin systems with trapped ions, Rev. Mod. Phys. **93**, 025001 (2021).

[85] C. Figgatt, A. Ostrander, N. M. Linke, K. A. Landsman, D. Zhu, D. Maslov, and C. Monroe, Parallel entangling operations on a universal ion-trap quantum computer, Nature (London) **572**, 368 (2019).

[86] D. F. James and J. Jerke, Effective Hamiltonian theory and its applications in quantum information, Can. J. Phys. **85**, 625 (2007).

[87] J. Zhang, M. Um, D. Lv, J.-N. Zhang, L.-M. Duan, and K. Kim, NOON States of Nine Quantized Vibrations in Two Radial Modes of a Trapped Ion, Phys. Rev. Lett. **121**, 160502 (2018).

[88] M. Um, J. Zhang, D. Lv, Y. Lu, S. An, J.-N. Zhang, H. Nha, M. Kim, and K. Kim, Phonon arithmetic in a trapped ion system, Nat. Commun. **7**, 1 (2016).

[89] H.-Q. Zhang, M.-Z. Ai, J.-M. Cui, Y.-J. Han, C.-F. Li, and G.-C. Guo, Investigating the quench dynamics of the bound states in a spin-orbital-coupling system using a trapped ion, Phys. Rev. A **104**, 022213 (2021).

[90] S.-J. Dong, W.-Y. Liu, C. Wang, Y. Han, G.-C. Guo, and L. He, TNSPackage: A Fortran2003 library designed for tensor network state methods, Comput. Phys. Commun. **228**, 163 (2018).